communications physics

Article

https://doi.org/10.1038/s42005-024-01913-1

Symmetry-governed dynamics of magnetic skyrmions under field pulses

Vladyslav M. Kuchkin [1] ✉, **Bruno Barton-Singer** [2], **Pavel F. Bessarab** [3,4] & **Nikolai S. Kiselev** [5] ✉

Topological magnetic solitons, such as skyrmions, exhibit intriguing particle-like properties that make them attractive for fundamental research and practical applications. While many magnetic systems can host skyrmions as statically stable configurations, chiral magnets stand out for their ability to accommodate a wide diversity of skyrmions with arbitrary topological charges and varied morphologies. Despite extensive investigation, a complete understanding of chiral magnetic skyrmions has remained elusive. We present a classification of all chiral skyrmions, demonstrating three classes based on their response to external magnetic field pulses: stationary, translating, and rotating. We highlight the role of magnetic texture symmetry in this classification. Skyrmions with varied dynamics offer avenues for exploring phenomena like skyrmion-skyrmion scattering that might be crucial for future applications.

Skyrmions are well-localized in space, topologically nontrivial magnetic textures, attractive for future information computing devices, from classical[1] to neuromorphic[2] and quantum[3]. Skyrmions were first predicted[4] and experimentally observed[5,6] in chiral magnets—a special type of materials characterized by competing Heisenberg exchange and Dzyaloshinskii-Moria interaction[7,8] (DMI). The prominent examples of chiral magnets are B20-type crystals, e.g., $\mathrm{Fe}_{1-x}\mathrm{Co}_x\mathrm{Si}$[6,9], FeGe[10–13], MnSi[5,14], and others compounds[15]. Besides that, skyrmions were also observed in many other magnetic crystals and heterostructures[1].

The whole family of chiral magnets can be roughly divided into three-dimensional (3D) and two-dimensional (2D) systems. Excluding apparent phenomena unique to 3D systems, e.g., the skyrmion braiding effect[16] or stability of chiral bobbers[17] and hopfion rings[18], many phenomena can occur both in 2D and 3D systems. A prominent example of such phenomena is the coexistence of skyrmions and antiskyrmions, which first was theoretically predicted by 2D model[19] and later were observed by means of Lorentz transmission electron microscopy (TEM) in a thin film of FeGe[20]. As such, the predictive capacity of the 2D model in chiral magnets provides a robust framework for anticipating effects across both 2D and 3D systems.

In the micromagnetic framework, the total energy of a thin plate of an isotropic chiral magnet can be written as follows:

$$\mathcal{E} = \int \{\mathcal{A}|\nabla \mathbf{n}|^2 + \mathcal{D} w_{\mathrm{D}}(\mathbf{n}) - M_{\mathrm{s}} \mathbf{B}_{\mathrm{ext}} \cdot \mathbf{n}\}\, \Delta l \, \mathrm{d}S, \tag{1}$$

where $\mathbf{n}$ is the magnetization unit vector field, M_{s} is the saturation magnetization of the material, $\mathcal{A}$ and $\mathcal{D}$ are the exchange stiffness constant and the DMI constant, respectively. Since we consider the 2D model, the magnetization field $\mathbf{n}$ is assumed uniform across the film thickness, Δl.

The DMI term $w_{\mathrm{D}}(\mathbf{n})$ is defined by combinations of Lifshitz invariants, $\Lambda_{ij}^{(k)} = n_i \partial_k n_j - n_j \partial_k n_i$. Without loss of generality, in our calculations, we assume Bloch-type DMI where $w(\mathbf{n}) = \Lambda_{zy}^{(x)} + \Lambda_{xz}^{(y)}$. However, the results presented here are also valid for systems with Néel-type modulations[21–23] as well as for crystals with $\mathrm{D}_{2\mathrm{d}}$ or S_4 point group symmetry[24,25].

The last term in (1) is the Zeeman interaction with the external magnetic field, which is assumed perpendicular to the plane of the film, $\mathbf{B}_{\mathrm{ext}} = B\mathbf{e}_z$. In a more particular case, the Hamiltonian (1) can also include the magnetocrystalline anisotropy and the demagnetizing field energy terms. These terms, however, do not change the presented results qualitatively, so we exclude them in favor of the simplicity. Moreover, we employ dimensionless units[4,26] of distances given with respect to the equilibrium period of chiral modulations at the ground state, $L_{\mathrm{D}} = 4\pi\mathcal{A}/\mathcal{D}$. The strength of the external magnetic field is given in units of the saturation field, $B_{\mathrm{D}} = \mathcal{D}^2/(2M_{\mathrm{s}}\mathcal{A})$. Here, we neglect the demagnetizing field in (1), as in the limit of an extended 2D plate with $\Delta l \to 0$, it can be treated as an effective easy-plane anisotropy and a rescaled external magnetic field. However, in Supplementary Note 1, we demonstrate the stability of various skyrmions considered in this work in the film of finite thickness and in the presence of the demagnetizing fields (see Supplementary Fig. 1).

---

[1]Department of Physics and Materials Science, University of Luxembourg, Luxembourg, Luxembourg. [2]Institute of Applied and Computational Mathematics, Foundation for Research and Technology - Hellas, Heraklion, Greece. [3]Science Institute, University of Iceland, Reykjavík, Iceland. [4]Department of Physics and Electrical Engineering, Linnaeus University, Kalmar, Sweden. [5]Peter Grünberg Institute, Forschungszentrum Jülich and JARA, Jülich, Germany.
✉e-mail: vladyslav.kuchkin@uni.lu; n.kiselev@fz-juelich.de

Recently, a series of works[27–35] reported the discovery of a wide diversity of magnetic skyrmions as statically stable solutions of the 2D model of chiral magnet. In Fig. 1a, we provide representative examples of such solutions, including skyrmion bags[27,28] and skyrmions with chiral kinks[29]. So-called tailed skyrmions, which were reported recently[30], are not shown in Fig. 1a but are also discussed in this study.

Until now, the dynamical properties of chiral magnetic skyrmions with arbitrary topological charge have been discussed mainly in the context of transnational motion induced by electric current[36–38]. It was shown that besides the topological charge,

$$Q = \frac{1}{4\pi}\int \mathbf{n}\cdot\left[\partial_{x}\mathbf{n}\times\partial_{y}\mathbf{n}\right]\mathrm{d}S, \tag{2}$$

which defines the skyrmion Hall effect, the rotational symmetry of skyrmions represents another important characteristic determining the dynamics[36]. The order of rotational symmetry k_s of a 2D localized magnetic texture is defined as the number of times the texture is transformed into itself when it undergoes a complete in-plane rotation. In other words, k_s is the maximum integer for which the following symmetry holds[36]:

$$\mathbf{n}(\mathbf{r}) = \mathcal{R}(\pm\phi)\,\mathbf{n}\big(\mathcal{R}(-\phi)\mathbf{r}\big), \tag{3}$$

where $\mathcal{R}(\phi)$ is the 3×3 rotation matrix about the z-axis by angle $\phi = 2\pi/k_s$. The sign $\pm$ in Eq. (3) accounts for different types of DMI [see Ref. 36 for details]. In the case of axially symmetric skyrmions, e.g., ordinary π-skyrmion and skyrmionium, one has $k_s = \infty$.

Here, we show that the whole family of 2D chiral magnetic skyrmions can be categorized into three classes based on skyrmion's topological index, Q, and its order of rotational symmetry, k_s [Fig. 1a]. Each class is characterized by a particular dynamics in response to a short pulse of external magnetic field. As we show below performing numerical simulations with the Landau-Lifshitz-Gilbert (LLG) equation, some skyrmions exhibit translational motion, some rotational motion and some skyrmions stay at rest without motion.

Results

External field pulse

It is well known that the motion of magnetic skyrmions can be induced by various stimuli, e.g., by a gradient of the internal parameters (for instance, $\mathcal{A}$, $\mathcal{D}$ or M_s) or by external parameters such as applied magnetic field[39], or temperature[40]. The translation motion of magnetic skyrmions also can be induced by electrical current[41,42], spin waves[43], etc. Here we consider the skyrmion dynamics induced by the short pulses of the perpendicular external magnetic field, $B_{\text{ext}}(t) = B_0 + \delta B(t)$, where B_0 is a constant magnetic field, and $\delta B(t) \ll B_0 < B_{\text{D}}$ is a small perturbation varying over time [Fig. 1b]. In the case of zero damping, $\alpha = 0$, the whole energy of the pulse is transferred to the magnetic texture dynamics, which, depending on the skyrmion type, can correspond to translational or rotational motion of the skyrmion [Fig. 1b]. For $\delta B(t) \ll B_{\text{D}}$, the translational or rotational velocity follows the same time dependence as $\delta B(t)$ [blue lines in Fig. 1b]. In this regime, the skyrmion is set in motion at the rising edge of the pulse and returns to rest at the falling edge of the pulse. Between the pulses, the skyrmion velocity remains constant, justifying an adiabatic approximation where we consider the steady-state velocity of a skyrmion in a static field.

In the case of finite damping, $\alpha > 0$, the behavior of the system will depend on the ratio between the interval between the rising and falling edges of pulses, Δt, and the relaxation time, t_r, which in the first approximation is inversely proportional to the damping parameter, $t_r \sim M_s(\gamma\alpha)^{-1}$. For a short interval between pulses, $\Delta t \ll t_r$, when the system is not able to reach relaxation, the velocity of the skyrmion might exhibit the sign flip for a short period of time. As in the case of zero damping, the resulting distance, r_s, traveled by the skyrmion in this case, will still be non-zero [red lines in Fig. 1b]. Thereby, two cases of $\alpha = 0$ and $0 < \alpha \ll 1$ are qualitatively identical.

On the contrary, in the case of $\Delta t \gtrsim t_r$, [green lines in Fig. 1b], the skyrmion reaches relaxation between the pulses and returns to its initial position after application of the second pulse. This scenario, which may naturally take place in the system with high damping, leads to the vibration of skyrmions—when the position of the skyrmion is changing in time, but the average distance traveled by skyrmion equals zero, $r_s = 0$. Note that all of the above is valid not only for translation but also for the rotational dynamics of skyrmions.

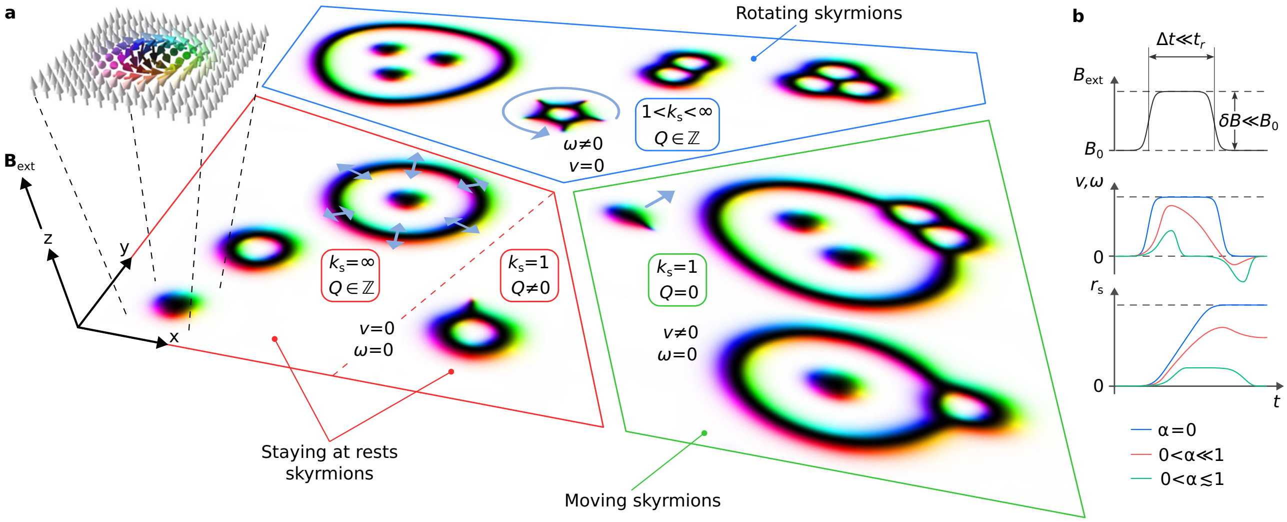

Fig. 1 | Three fundamental classes of chiral magnetic skyrmions. a shows diverse solutions of chiral magnetic solitons in 2D that can be decomposed into three classes based on their response to a step-like pulse of the external magnetic field. The order of the skyrmion rotation symmetry (k_s) and skyrmion topological charge Q uniquely define the skyrmion dynamical class. Topologically trivial solutions with low symmetry, $Q = 0$ and $k_s = 1$, belong to the class of solitons moving with constant linear velocity, $v \neq 0$. The high symmetry skyrmions with $1 < k_s < \infty$ are the solitons rotating about their geometrical center with constant angular velocity, $\omega \neq 0$. All other skyrmions belong to the class of solitons, which exhibit the breathing mode only, with $v = 0$ and $\omega = 0$. The top-left zoom-in schematically illustrates the magnetic vector field of a π-skyrmion and explains the standard color code used throughout the paper: white and black pixels represent magnetic moments aligned parallel and antiparallel to the z-axis, respectively, while red, green, and blue indicate the azimuthal angle relative to the x-axis. **b** shows the magnetic field pulse $\delta B(t)$ and the dynamical response of the solitons: velocity (v, ω) and collective coordinate r_s as a function of time. Dependencies v, ω, r_s on time are different for various dissipation regimes: zero damping (blue), infinitesimally small damping (red), and strong damping (green).

The results presented in this work are based on the nondissipative dynamics approach, which, as we have mentioned above, remain qualitatively equivalent to the case of small damping, $0 < \alpha \ll 1$, and short pulses. Numerical simulations of such skyrmion dynamics were performed in Mumax[44] with Gilbert damping, α, set to zero. To ensure that the whole energy of the pulse is transferred into skyrmion motion, we use pulses of a smooth profile and very weak intensity, $\delta B = 0.01 B_D$. Otherwise, the field pulse can excite combined vibrational translational motion modes, which may even lead to skyrmion instability. In most cases, we succeed in decoupling two types of excitations. However, in some cases, it has proved impossible to completely avoid the coupling between translational and vibrational modes. Such cases are discussed separately in the text.

Symmetry analysis

The skyrmion behavior observed in the numerical experiment and summarized in Fig. 1 can be understood using the collective coordinate approach. In the literature, this approach, based on the assumption of rigid translation or rotation of magnetic solitons, is also known as the Thiele approach[45]. For further convenience, we parametrize magnetization using the spherical angles, $n = (\sin\Theta\cos\Phi, \sin\Theta\sin\Phi, \cos\Theta)$ and consider translational and rotational motion of skyrmions separately.

In the case of translational motion induced by external field pulse, the corresponding equation of motion can be written as $\Phi(\mathbf{r}, t) = \Phi(\mathbf{r} - \boldsymbol{v}t)$ and $\Theta(\mathbf{r}, t) = \Theta(\mathbf{r} - \boldsymbol{v}t)$ where $\boldsymbol{v} = (v_x, v_y)$ is a slowly-varying in time velocity of skyrmion. The velocity $\boldsymbol{v}$ should satisfy the Thiele equation[45]:

$$\mathbf{e}_z \times \boldsymbol{v} \int q \mathrm{d}S = 0, \tag{4}$$

where $q = (4\pi)^{-1}\left(\partial_x\Theta\partial_y\Phi - \partial_y\Theta\partial_x\Phi\right)\sin\Theta$ is the topological charge density. It is worth emphasizing that the Thiele equation is derived from the energy conservation law.

In the case of rotational motion, the dynamics of magnetic texture can be described as $\Phi(x, y, t) = \Phi(x', y') - \omega t$ and $\Theta(x, y, t) = \Theta(x', y')$, where ω is the angular velocity and (x', y') are rotated coordinates:

$$x' = x\cos\omega t - y\sin\omega t,\ \ y' = y\cos\omega t + x\sin\omega t. \tag{5}$$

In this case, the Thiele equation can be written as[46]:

$$\omega\int qx\mathrm{d}S = 0,\ \ \omega\int qy\mathrm{d}S = 0. \tag{6}$$

Interestingly, equations (4) and (6) can only yield non-trivial solutions ($\boldsymbol{v} \neq 0$ or $\omega \neq 0$) when the corresponding integrals of q, qx, and qy are zero. In the next sections, we provide the exact equations for these velocities by considering an approach that goes beyond the Thiele approximation. However, to distinguish magnetic skyrmions by their dynamics from the very general perspective, it is enough to consider Eqs. (4) and (6). In particular, assuming a skyrmion satisfies either Eq. (4) or Eq. (6), we can categorize skyrmions into three types based on their rotational symmetry order, k_s, and topological charge, Q.

Let us start with Eq. (6) for skyrmion rotation. The charge density q has the same rotation symmetry as the corresponding magnetization field, and can be written as a Fourier series in polar coordinates $(x, y) = (\rho\cos\phi, \rho\sin\phi)$. It is easy to show that $q \sim a\cos(k_s\phi) + b\sin(k_s\phi)$ and thus the necessary condition of zeroing integrals qx and qy in (6) is $k_s > 1$. Thereby, low-symmetry skyrmions with $k_s = 1$ cannot rotate with fixed angular velocity because, in this case, Eq. (6) has only one solution, $\omega = 0$. On the other hand, any high symmetry skyrmions with $k_s \geq 2$ possess the ability to rotate. The aforementioned criterion applies to skyrmions of any arbitrary topological charge, including topologically trivial solitons. Finally, it is worth noting that in the case of axially symmetric solutions, $k_s = \infty$, the angular velocity ω, is ill-defined. The latter is easy to understand since, for an axially symmetric soliton in a perpendicular field, there are no orientational parameters, and all directions are equivalent. Because of that, all axially symmetric skyrmions must be excluded from the first class of solutions characterized by rotational motion.

Now let us consider the second class of solutions for skyrmions, which satisfies Eq. (4) for translational motion. It is evident that to make the integral in (4) equal to zero, the skyrmion must be topologically trivial, $Q = 0$. On the other hand, the solutions with $Q = 0$ formally satisfy the above criteria for rotating skyrmions when they have a high symmetry. The only solutions, which do not overlap with the first class are the topologically trivial $Q = 0$, skyrmions with single-fold symmetry, $k_s = 1$. In the next section, we provide more rigorous arguments in favor of this statement.

The third class is composed of all the other skyrmions that do not satisfy the criteria for the first and second classes. All axially symmetric solutions belong to this class irrespective of the topological charge. Besides that, all low-symmetry skyrmions with $k_s = 1$ and nonzero topological charges, $Q \neq 0$, also belong to the third class. In agreement with the above, the numerical simulations show that the magnetic field pulses cannot induce either rotation or translation of these skyrmions. Magnetic field pulses excite only self-vibrating modes of such skyrmions, which can be effectively suppressed by using smooth profile pulses [Supplementary Movie 1].

Skyrmion velocities

The classification of chiral skyrmions outlined in the previous section is qualitative. The latter means that the exact values for the linear, v, and angular, ω, skyrmion velocities, do not follow from the Thiele equations (4), (6). Deriving analytical expressions for velocities and their dependencies on the model parameters, e.g., pulse intensity, δB, requires going beyond the Thiele approach. One way of doing that is to take into account the conservation of other quantities rather than energy conservation as in the original Thiele approach. Earlier, Papanicolaou and Tomaras showed[46] that at zero damping, a linear momentum conservation law holds for moving solitons and a angular momentum conservation law holds for rotating solitons. In Supplementary Note 2, we derive the following equations for translational skyrmion motion:

$$\boldsymbol{v}\cdot\boldsymbol{p} = -\gamma m\delta B, \tag{7}$$

and for skyrmion rotation:

$$\omega(l + m) = -\gamma m\delta B. \tag{8}$$

In (7) and (8), γ is the gyromagnetic ratio, m is remanent magnetization along the z-axis, $\boldsymbol{p}$ is the skyrmion linear momentum, l is the skyrmion angular momentum which can be written as follows[46]:

$$\boldsymbol{p} = \int \mu\left(\mathbf{e}_x\frac{\partial\Phi}{\partial x} + \mathbf{e}_y\frac{\partial\Phi}{\partial y}\right)\mathrm{d}S, \tag{9}$$

$$l = \int \mu\left(y\frac{\partial\Phi}{\partial x} - x\frac{\partial\Phi}{\partial y}\right)\mathrm{d}S, \tag{10}$$

where $\mu = (4\pi)^{-1}(1 - \cos\Theta)$ is magnon density. Since equations (7) and (8) are linear with respect to velocities, they are straightforward to solve. However, the calculation of the momentum integrals, $\boldsymbol{p}$ and l in (9), (10) (Supplementary Note 3), may present a challenge. Nevertheless, in some simple cases discussed in the following section, $\boldsymbol{p}$ and l can be easily calculated. Furthermore, one can demonstrate a connection between the momenta $\boldsymbol{p}$ and l and the topological charge density q [Supplementary Note 3].

One of the advantages of Eqs. (7) and (8) is that contrary to the original Thiele equation, they can describe the dynamics where the velocities are allowed to change in time. The latter, however, is true for negligibly small damping only. Moreover, it is important to emphasize that Eqs. (7) and (8) can be used only together with the above symmetry analysis and skyrmion classification based on Thiele equations (4) and (6). The above statement can be illustrated as follows. Let us consider any axially symmetric skyrmion, which, according to the symmetry analysis of Thiele equations and numerical experiment, exhibits neither rotational ($\omega = 0$) nor translational motion ($v = 0$). The formal nonzero solutions of (7) and (8), in this case, do not have a physical meaning.

The dynamics of the most compact skyrmions

As follows from (7), (8), translational ($\boldsymbol{v}$) and angular (ω) velocities are linearly proportional to the field pulse, δB. Proportionality coefficients represent $\boldsymbol{p}$ and l, the values of which are not so obvious since the corresponding integrals in (9), (10) depend on the details of the skyrmion structure. As it was shown in Ref. 46, for skyrmions with *simple cores*, the momenta $\boldsymbol{p}$ and l can be calculated straightforwardly. By *simple cores*, we assume that the regions with $n_z = -1$ represent points. In the opposite case, when the regions with $n_z = -1$ represent extended segments, e.g., closed lines, arcs, etc., we say that the skyrmion has *complex cores*.

The most compact skyrmions characterized by the presence of only simple cores are depicted in Fig. 2a–c. The π-skyrmion with $Q = -1$ depicted in **a** belongs to the class of resting solitons, the chiral droplet[47] with $Q = 0$ in **b** belongs to moving solitons, and the antiskyrmion[19] with $Q = 1$ in **c** belongs to the class of rotating skyrmions. As follows from the magnetization profiles, the π-skyrmion, chiral droplet and antiskyrmion have one, two, and three simple cores, respectively.

According to our classification, only the droplet and antiskyrmion can demonstrate pulse-induced motion. In the numerical experiment, we estimated the velocities of the chiral droplet and antiskyrmion for various pulse strengths (Method). In Fig. 2d, e, we provide this data together with the solutions of Eqs. (7), (8) for comparison. We observe a good agreement for small pulse amplitude. The snapshots of the droplet and antiskyrmion at different times are depicted in **f** and **g**, respectively. For the chosen parameters (Method), the droplet linear velocity is $\sim 1.7 m/s$, and the antiskyrmion angular velocity is ~ 70 MHz.

Dynamics of skyrmion bags, kinked and tailed skyrmions

To illustrate the validity of the above classification, we examined a large variety of statically stable solutions that were predicted before[27–31]. For instance, Fig. 3a–e show the set of topologically trivial skyrmions with single-fold symmetry, $k_s = 1$. Supplementary Movie 2 illustrates the dynamics of skyrmions depicted in Fig. 3a–e and the droplet soliton after applying the pulse. Comparison of the velocities allows us to deduce that the 3π-skyrmion with chiral kink depicted in **a** has the highest speed, 2.01 m/s among all other skyrmions. Note, that all textures depicted in Fig. 3 are stabilized at slightly different applied fields, but their dynamics are induced by the pulse of the same amplitude, δB.

Skyrmions **a**–**d** have a *mirror* symmetry (see Supplementary Fig. 2) with respect to line $x = y$. The linear velocity of such skyrmions is always pointing perpendicular to the mirror axis [Supplementary Note 3]. The example of a solution with a lack of such mirror symmetry is given in **e**.

For the skyrmionium with a tail depicted in **c**, we observe the presence of additional vibrations. We explain such vibration by the excitation of a skyrmion breathing mode. In the case of other skyrmions, the presence of such vibrations is much less prominent and can be thought of as a small perturbation on top of the main type of dynamics. The excitation of these modes can be suppressed by applying a smoother pulse shape. That means that the transition from B_0 to $B_0 + \delta B$ is more extended in time, similar to what is indicated in Supplementary Movie 1. In the case of tailed skyrmions, a smooth shape profile may not be sufficient, and one has to reduce the pulse amplitude in addition.

Different high-symmetry rotating skyrmions are shown in Fig. 3f–j. The skyrmion bag in **f** and skyrmion with chiral kinks on the inner shell in **i**

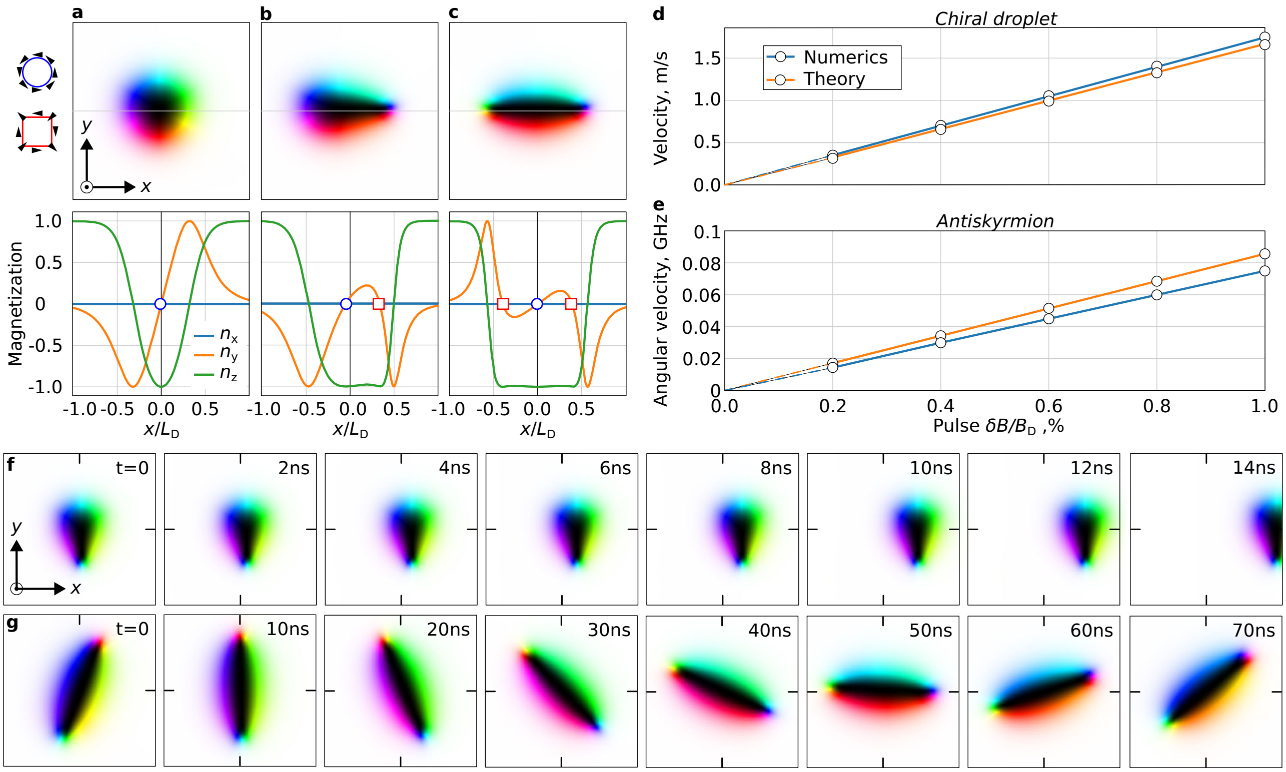

Fig. 2 | The most compact skyrmions of the three classes. **a**–**c** shows magnetic textures of the π-skyrmion, chiral droplet, and antiskyrmion stabilized at magnetic field $h = 0.62$. The magnetization components $\mathbf{n}(x)$ along the line $y = 0$ are shown below. Hollow circles and squares denote the position of solitons' cores $n_x = n_y = 0$ and $n_z = -1$ with winding $\nu = +1$ and $\nu = -1$, respectively, as provided in the top left inset. **d** and **e** show the comparison between velocities obtained in simulations and found analytically for the chiral droplet and antiskyrmion for the pulses of various amplitude. Dynamics for those solitons excited by the pulse $\delta B = 0.01 B_D$ can be seen from **f** and **g** providing the system snapshots at different times. For the color code used in panels **a**–**c**, **f** and **g**, we refer the reader to the top-left zoom-in in Fig. 1a.

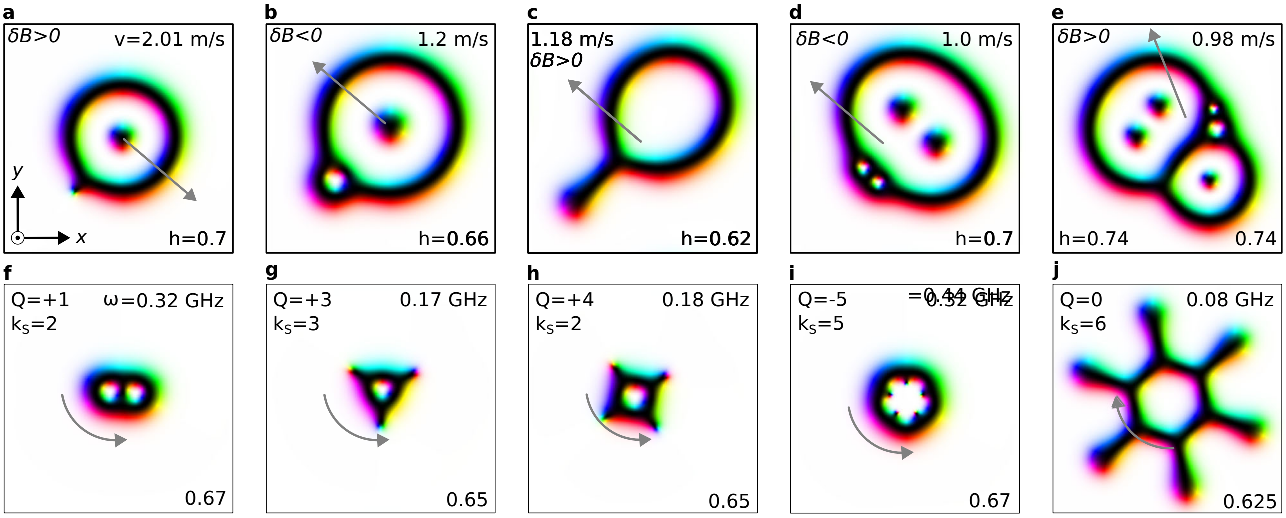

Fig. 3 | Dynamics of moving and rotating skyrmions. **a**–**e** shows examples of topologically trivial skyrmions ($Q = 0$) with $k_s = 1$. **f**-**j** show the magnetic skyrmions with $k_s > 1$. All states are stabilized at given magnetic fields, h. Gray arrows show the direction of the motion. The provided values of skyrmion velocities correspond to the pulse $|\delta B| = 0.01B_D$. For the color code used in panels **a**–**j**, we refer the reader to the top-left zoom-in in Fig. 1a.

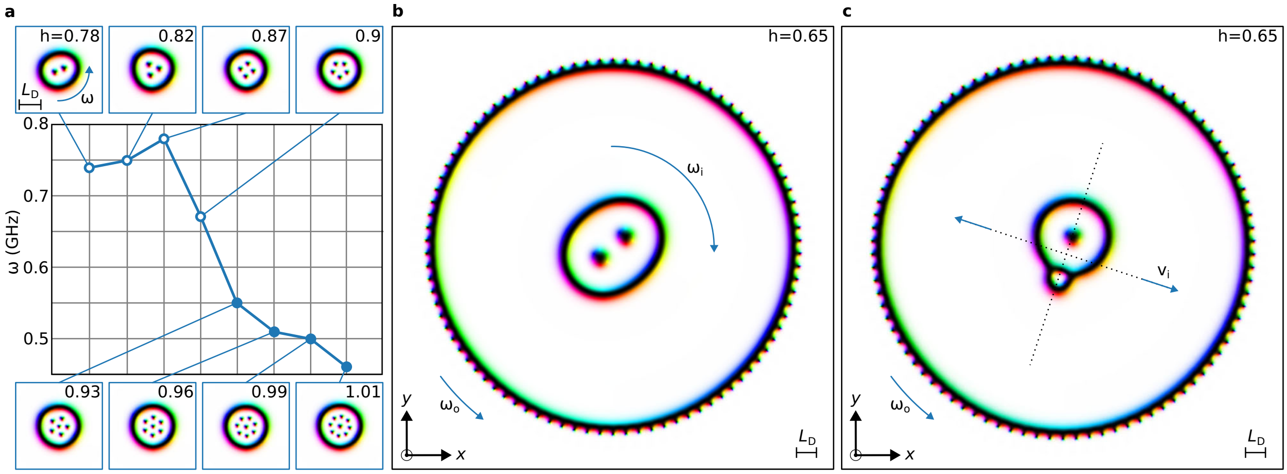

Fig. 4 | Complex rotational dynamics of skyrmion bags. **a** shows angular velocity, ω, for a set of high-symmetry skyrmion bags stabilized at various magnetic fields $h = B_{\text{ext}}/B_D$. The field values indicated in each inset are chosen to achieve bags of nearly same sizes. All inset images have identical sizes of $4L_D \times 4L_D$. **b** and **c** show nested skyrmion bags which exhibit more complex dynamics. In both cases, the outer bag, which contains multiple chiral kinks, rotates counterclockwise with angular velocity ω_o. The inner skyrmion bag either rotates clockwise with angular velocity ω_i as in **b** or moves with linear velocity v_i as in **c**. Due to the interaction with the outer skyrmion bags, the inner skyrmion in **c** exhibits back-and-forth motion. For the color code used in panels **a**-**c**, we refer the reader to the top-left zoom-in in Fig. 1a.

have the highest angular velocities, ~0.32 GHz. Skyrmion bags with chiral kinks on the outer shell depicted in **g** and **h** rotate with almost twice smaller angular velocity, $\omega = 0.17$ GHz and 0.18 GHz, respectively. The skyrmionium with tails depicted on **j** has the lowest angular velocity. The dynamics of rotated skyrmions is illustrated in Supplementary Movie 3.

From results provided in Fig. 3f–j we can deduce that skyrmion bags are good candidates for the fastest-rotating skyrmions. We studied various skyrmion bags with positive and negative topological charges to explore this conjecture more systematically. We concluded that for achieving the maximum ω, skyrmion bags with negative Q are more efficient.

To keep all these skyrmion bags depicted in Fig. 4 approximately the same size, one must apply different magnetic fields. The solutions can be divided into two groups depending on the absence (open symbols) of the presence (solid symbols) of the π-skyrmion in the center of the bag. Although this classification is somewhat arbitrary, the angular velocities of skyrmion bags from these two groups are quite different. For the chosen micromagnetic parameters, the skyrmion bag in **c** has the highest angular velocity $\omega = 0.78$ GHz. The rotation of skyrmion bags depicted in Fig. 4 is illustrated in Supplementary Movie 4. It is worth noting that in these simulations, we utilized high-order discretization schemes for numerical calculation of spatial derivatives in the Hamiltonian (1) and effective field terms in the LLG equation[36].

The wide diversity of skyrmion bags of different sizes and symmetry stabilized at identical conditions allows the study of complex dynamics beyond ordinary rotational or translational motion. Such complex dynamics can be observed, for instance, when one skyrmion bag is nested inside another skyrmion bag of larger size, as depicted in Fig. 4b and c. The size of the outer skyrmion bag can be controlled by the number of attached chiral kinks, which tend to be equidistantly distributed with period ~ $1L_D$ along the perimeter. The applied magnetic field pulse excites the rotational motion of the outer high-symmetry skyrmion bag. When the inner skyrmion also has high-symmetry $k_s > 1$, as in Fig. 4b, it also rotates. However, the rotation directions of the inner and outer skyrmion bags do not necessarily coincide. Decreasing the diameter of the outer skyrmion bag, such as by reducing the number of chiral kinks and allowing closer interaction between the inner and outer skyrmion bags, will affect their angular velocities. Below the critical size of the outer skyrmion bag, the angular velocity of the inner skyrmion can even change the sign, as illustrated in Supplementary Movie 5.

If the inner skyrmion is topologically trivial and has $k_s = 1$ as in Fig. 4c, the applied magnetic field pulse will excite its translational motion. Since the center of the outer skyrmion ring is fixed, at some point, the inner skyrmion starts to interact with the outer skyrmion bag. As a result of elastic interaction between skyrmions, the linear velocity v_i of the inner skyrmion changes the direction, which leads to the back-and-forth motion of the inner skyrmion bag. Supplementary Movie 6 illustrates the dynamics of skyrmion bags depicted in Fig. 4b, c.

Skyrmion-skyrmion scattering

The different dynamical response of skyrmions to the magnetic field pulse provides a unique opportunity to study skyrmion scattering process. To illustrate this effect, in Fig. 5 we show the results of micromagnetic simulations for chiral droplet and the π-skyrmion. We select chiral droplet and π-skyrmion as most compact solitons in the class of moving and resting skyrmions, respectively. Thereby, π-skyrmion represents a *target particle*, and the chiral droplet plays the role of a *bullet particle*.

In the absence of the π-skyrmion, the trajectories of the chiral droplet represent straight lines (see dashed lines in Fig. 5a). In our setup, this line is parallel to the x-axis. We conducted a series of micromagnetic simulations with different *impact parameter*. While the observed interaction shares similarities with Rutherford's scattering, the functional dependence of the deflection angle on the impact parameter is distinctly different. In particular, we found that deflection angle β can change its sign depending on the impact parameter. Our estimation suggests that the critical distance, where the deflection angles abruptly change sign, occurs at $\sim 2L_D$. To elucidate this deflection angle behavior, one must consider interparticle interaction potentials like those discussed in Refs. 19,32 regarding skyrmion-antiskyrmion interaction. However, an in-depth exploration of this topic falls outside the scope of this work. Our primary objective here is to introduce the external field pulse excitations as a promising approach for investigating the scattering processes of chiral skyrmions.

Even more elaborate scattering processes occur when the target particle is a soliton that can move. Supplementary Movie 7 illustrates the three most representative cases of skyrmion scattering. An interesting effect occurs when a topologically trivial skyrmionium is the target particle. According to the above classification, the applied pulse cannot induce skyrmionium motion, but interaction with the bullet particle can. This statement is in agreement with Eq. (4). The direction of skyrmionium motion is primarily defined by the impact parameter between the droplet and the target. The linear momentum conservation law holds in this case. As seen in Supplementary Movie 7, the speed of the chiral droplet decreases after partially transferring its linear momentum to the skyrmionium.

Similar to the droplet's scattering on the π-skyrmion, the scattering on a rotating skyrmion bag resembles the elastic scattering of particles. It is intriguing that the dynamics of magnetic skyrmions, described by first-order differential equations with respect to time, exhibit so many similarities to the dynamics of Newtonian particles, which are described by second-order differential equations with respect to time. On the other hand, there are many differences. For instance, besides the aforementioned flip of the scattering angle sign [Fig. 5], it is noticeable that the angular velocity of the skyrmion bag does not change when it interacts with the chiral droplet (see Supplementary Movie 7). These and other effects related to skyrmion-skyrmion scattering require a separate study, which will be presented elsewhere.

Conclusions

We have studied the magnetic field pulse-induced dynamics of 2D chiral magnetic skyrmions. The observed phenomenon, however, is not limited to chiral magnets and applies to all 2D magnetic systems that support topological magnetic solitons irrespective of the underlying Hamiltonian. Moreover, the presented results remain valid for arbitrary external excitations that effectively act as a magnetic field pulse, e.g., laser pulses, in zero and weak damping regimes. It is shown that, based on their symmetry and topological index, all chiral skyrmions can be divided into three classes: breathing, moving, and rotating skyrmions. We have demonstrated that high-symmetry skyrmions can rotate with GHz-order frequency.

We have shown that skyrmion velocities can be calculated semi-analytically using the derived equations, which are consistent with the conservation laws of angular and linear momentum. Additionally, we illustrate the complex dynamics of nested skyrmion bags. Finally, we investigated skyrmion scattering on different targets and showed that, while there are some similarities with Rutherford scattering, skyrmion-skyrmion scattering is generally a much more complicated phenomenon.

Methods

Micromagnetic simulations

Micromagnetic simulations were performed in Mumax[44]. The standard cuboid size in our simulations was 1 nm × 1 nm × 1 nm. The DMI constant is set such that the equilibrium period of helical modulations equals $L_D = 4\pi\mathcal{A}/\mathcal{D} = 64$ nm. All simulations are performed assuming periodical boundary conditions (PBC) in xy-plane. To increase the accuracy of the

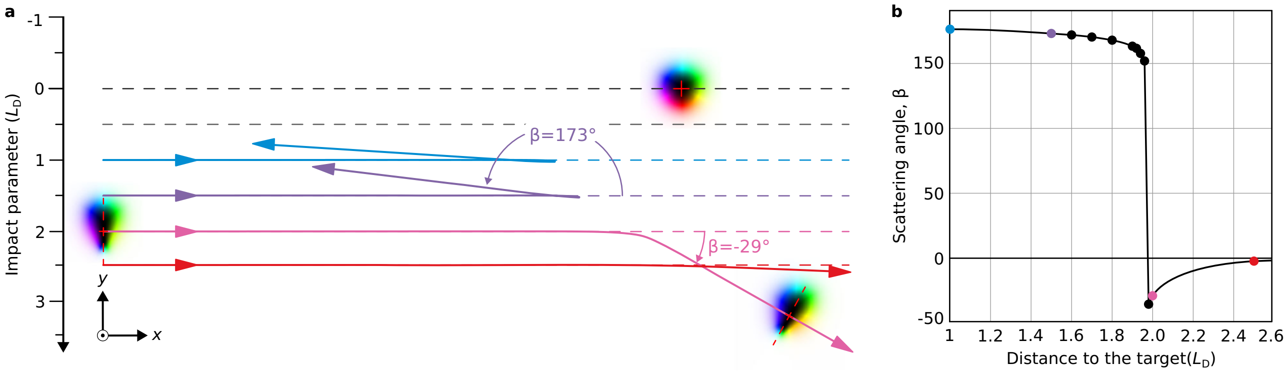

Fig. 5 | Pulse-induced skyrmion scattering. a shows the trajectories of the chiral droplet (bullet particle) at different distances to the π-skyrmion (target particle). For the distance of $2L_D$, we show the chiral droplet at two distinct points on its trajectory to illustrate its rotation during scattering. Such an interaction process is characterized by the scattering angle, $\beta \in [-180^\circ, 180^\circ]$. **b** shows the dependency of the angle β for different distances between bullet and target. The discontinuity in this dependency corresponds to a distance of $1.97L_D$. For the color code used in panel **a**, we refer the reader to the top-left zoom-in in Fig. 1a.

micromagnetic simulations, in some cases, we employed a fourth-order finite difference scheme in the calculation of the energy and effective field terms[27,36,48]. For details on implementing the finite difference scheme, see Supplementary Software file 1.

The dynamics discussed in the main text have been excited by pulses of the external magnetic field applied perpendicular to the magnetic film, $\delta B(t)$, defined as follows

$$\delta B(t) = A\left(1 - \frac{1+\exp(-\nu t_0)}{1+\exp(\nu(t-t_0))}\right), \tag{11}$$

with amplitude $A = 0.01B_{\mathrm{D}}$, time scaling factor $\nu = 1$ GHz and time offset, $t_0 = 10$ ns. It is worth noting that we use a single step-like field function.

Estimation of velocities from micromagnetic simulations

To estimate the linear velocity of skyrmion, we trace its position, $(x_{\mathrm{s}}, y_{\mathrm{s}})$, using the following formula optimized for the simulations with PBC[36]:

$$x_{\mathrm{s}} = \frac{L_{\mathrm{x}}}{2\pi}\arctan\left(\frac{\int \mathcal{N}_{\mathrm{y}} \sin\left(2\pi x/L_{\mathrm{x}}\right)\mathrm{d}x}{\int \mathcal{N}_{\mathrm{y}} \cos\left(2\pi x/L_{\mathrm{x}}\right)\mathrm{d}x}\right) \pm l_{\mathrm{x}}L_{\mathrm{x}}, \tag{12}$$

$$y_{\mathrm{s}} = \frac{L_{\mathrm{y}}}{2\pi}\arctan\left(\frac{\int \mathcal{N}_{\mathrm{x}} \sin\left(2\pi y/L_{\mathrm{y}}\right)\mathrm{d}y}{\int \mathcal{N}_{\mathrm{x}} \cos\left(2\pi y/L_{\mathrm{y}}\right)\mathrm{d}y}\right) \pm l_{\mathrm{y}}L_{\mathrm{y}}, \tag{13}$$

where $\mathcal{N}_{\mathrm{x}} \equiv \mathcal{N}_{\mathrm{x}}(y) = \int(1-n_{\mathrm{z}})\mathrm{d}x$ and $\mathcal{N}_{\mathrm{y}} \equiv \mathcal{N}_{\mathrm{y}}(x) = \int(1-n_{\mathrm{z}})\mathrm{d}y$. The integer numbers l_{x} and l_{y} account for crossing the domain boundary in the x and y directions, respectively. The sign (±) indicates the positive or negative direction of skyrmion motion along the corresponding axis. Knowing the skyrmion's position at any moment in time, the estimation of its velocity is straightforward.

For calculation of the angular velocity, ω, we first determine the number k_{s} for each soliton and then perform the Fourier transformations in polar coordinates:

$$\begin{aligned} m_{\mathrm{c}}(t) &= \int_0^{2\pi}(1-\cos\Theta(r,\phi,t))\cos(k_{\mathrm{s}}\phi)r\mathrm{d}r\mathrm{d}\phi, \\ m_{\mathrm{s}}(t) &= \int_0^{2\pi}(1-\cos\Theta(r,\phi,t))\sin(k_{\mathrm{s}}\phi)r\mathrm{d}r\mathrm{d}\phi. \end{aligned} \tag{14}$$

Both functions, $m_{\mathrm{c}}(t)$, $m_{\mathrm{s}}(t)$ represent harmonic functions of period $1/\omega$ which can be employed to find ω accurately. Due to the fact that simulations are done on the rectangular domain, integration in (14) can be done in Cartesian coordinates. For this purpose, we rewrite trigonometric functions as follows,

$$\begin{aligned} \sin(k_{\mathrm{s}}\phi) &= \frac{1}{r^{k_{\mathrm{s}}}}\sum_{n=0}^{\lfloor (k_{\mathrm{s}}-1)/2\rfloor}(-1)^n C_{k_{\mathrm{s}}}^{2n+1} x^{k_{\mathrm{s}}-2n-1} y^{2n+1}, \\ \cos(k_{\mathrm{s}}\phi) &= \frac{1}{r^{k_{\mathrm{s}}}}\sum_{n=0}^{\lfloor k_{\mathrm{s}}/2\rfloor}(-1)^n C_{k_{\mathrm{s}}}^{2n} x^{k_{\mathrm{s}}-2n} y^{2n}, \end{aligned} \tag{15}$$

where $C_a^b = a!/b!(a-b)!$ is the binomial coefficient.

Data availability

All relevant data are available from the corresponding author upon request.

Received: 26 June 2024; Accepted: 11 December 2024;

References

1. Tokura, Y. & Kanazawa, N. Magnetic skyrmion materials. *Chem. Rev*. **121** 5 (2020).
2. Song, K. M. et al. Skyrmion-based artificial synapses for neuromorphic computing. *Nat Electron* **3**, 148–155 (2020).
3. Psaroudaki, C. & Panagopoulos, C. Skyrmion qubits: a new class of quantum logic elements based on nanoscale magnetization. *Phys. Rev. Lett.* **127**, 067201 (2021).
4. Bogdanov, A. N. & Yablonskii, D. A. Thermodynamically stable "vortices" in magnetically ordered crystals. The mixed state of magnets. *Sov. Phys. JETP* **68**, 101 (1989).
5. Mühlbauer, S. et al. Skyrmion lattice in a chiral magnet. *Science* **323**, 915–919 (2009).
6. Yu, X. Z. et al. Real space observation of a two-dimensional skyrmion crystal. *Nature* **465**, 901 (2010).
7. Dzyaloshinsky, I. A thermodynamic theory of "weak" ferromagnetism of antiferromagnetics. *J. Phys. Chem. Solids* **4**, 241 (1958).
8. Moriya, T. Anisotropic superexchange interaction and weak ferromagnetism. *Phys. Rev.* **120**, 91 (1960).
9. Park, H. S. et al. Observation of the magnetic flux and three-dimensional structure of skyrmion lattices by electron holography. *Nat. Nanotechnol.* **9**, 5 (2014).
10. Yu, X. Z. et al. Near room-temperature formation of a skyrmion crystal in thin-films of the helimagnet FeGe. *Nat. Mater.* **10**, 106 (2011).
11. Kovács, A. et al. Mapping the magnetization fine structure of a lattice of Bloch-type skyrmions in an FeGe thin film. *Appl. Phys. Lett.* **111**, 192410 (2017).
12. Du, H. et al. Interaction of Individual Skyrmions in a nanostructured cubic chiral magnet. *Phys. Rev. Lett.* **120**, 19 (2018).
13. Yu, X. et al. Aggregation and collapse dynamics of skyrmions in a non-equilibrium state. *Nat. Phys.* **14**, 8 (2018).
14. Yu, X. et al. Variation of skyrmion forms and their stability in MnSi thin plates. *Phys. Rev. B* **91**, 5 (2015).
15. Shibata, K. et al. Towards control of the size and helicity of skyrmions in helimagnetic alloys by spin–orbit coupling. *Nat. Nanotechnol.* **8**, 10 (2013).
16. Zheng, F. et al. Magnetic skyrmion braids. *Nat. Commun.* **12**, 5316 (2021).
17. Zheng, F. et al. Experimental observation of chiral magnetic bobbers in B20-type FeGe. *Nat. Nanotech.* **13**, 451–455 (2018).
18. Zheng, F. et al. Hopfion rings in a cubic chiral magnet. *Nature* **623**, 718–723 (2023).
19. Kuchkin, V. M. & Kiselev, N. S. Turning a chiral skyrmion inside out. *Phys. Rev. B* **101**, 064408 (2020).
20. Zheng, F. et al. Skyrmion-antiskyrmion pair creation and annihilation in a cubic chiral magnet. *Nat. Phys.* **18**, 863–868 (2022).
21. Romming, N. et al. Writing and deleting single magnetic skyrmions. *Science* **341**, 636 (2013).
22. Kézsmárki, I. et al. Néel-type skyrmion lattice with confined orientation in the polar magnetic semiconductor GaV4S8. *Nat. Mater.* **14**, 1116 (2015).
23. Romming, N., Kubetzka, A., Hanneken, C., von Bergmann, K. & Wiesendanger, R. Field-dependent size and shape of single magnetic skyrmions. *Phys. Rev. Lett.* **114**, 177203 (2015).
24. Kosuke, K. et al. Room-temperature antiskyrmions and sawtooth surface textures in a non-centrosymmetric magnet with S_4 symmetry. *Nat. Mater.* **20**, 335–340 (2021).
25. Tang, J. et al. Sewing skyrmion and antiskyrmion by quadrupole of Bloch points. *Sci. Bull.* **68**, 2919–2923 (2023).
26. Bogdanov, A. & Hubert, A. The stability of vortex-like structures in uniaxial ferromagnets. *J. Magn. Magn. Mater.* **195**, 182 (1999).
27. Rybakov, F. N. & Kiselev, N. S. Chiral magnetic skyrmions with arbitrary topological charge. *Phys. Rev. B* **99**, 064437 (2019).
28. Foster, D. et al. Two-dimensional skyrmion bags in liquid crystals and ferromagnets. *Nat. Phys.* **15**, 655 (2019).
29. Kuchkin, V. M. et al. chiral kinks and holomorphic functions. *Phys. Rev. B* **102**, 144422 (2020).
30. Kuchkin, V. M., Kiselev, N. S., Rybakov, F. N., & Bessarab, P. F. Tailed skyrmions – An obscure branch of magnetic solitons. *Front. Phys*. **11** (2023).

31. Barton-Singer, B., Ross, C. & Schroers, B. J. Magnetic skyrmions at critical coupling. *Commun. Math. Phys.* **375**, 2259 (2020).
32. Barton-Singer, B. & Schroers, B. J. Stability and asymptotic interactions of chiral magnetic skyrmions in a tilted magnetic field. *SciPost Phys.* **15**, 011 (2023).
33. Wang, X. R., Hu, X. C. & Wu, H. T. Stripe skyrmions and skyrmion crystals. *Commun. Phys.* **4**, 142 (2021).
34. Hu, Xu-Chong, Wu, Hai-Tao & Wang, X. R. A theory of skyrmion crystal formation. *Nanoscale* **14**, 7516–7529 (2022).
35. Wang, X. R. & Hu, X. C. Particle-continuum duality of skyrmions. *Phys. Rev. B* **107**, 174412 (2023).
36. Kuchkin, V. M. et al. Geometry and symmetry in skyrmion dynamics. *Phys. Rev. B* **104**, 165116 (2021).
37. Kind, C. & Foster, D. Magnetic skyrmion binning. *Phys. Rev. B.* **103**, L100413 (2021).
38. Zeng, Z. et al. Dynamics of skyrmion bags driven by the spin-orbit torque. *Appl. Phys. Lett.* **117**, 172404 (2020).
39. Malozemoff, A. P. & Slonczewski, J. C. *Magnetic Domain Walls in Bubble Materials* (Academic Press, New York, 1979).
40. Kong, L. & Zang, J. Dynamics of an insulating skyrmion under a temperature gradient. *Phys. Rev. Lett.* **111**, 067203 (2013).
41. Jonietz, F. et al. Spin transfer torques in MnSi at ultralow current densities. *Science* **330**, 1648 (2010).
42. Zang, J., Mostovoy, M., Han, J. H. & Nagaosa, N. Dynamics of Skyrmion crystals in metallic thin films. *Phys. Rev. Lett.* **111**, 136804 (2011).
43. Schütte, C. & Garst, M. Magnon-Skyrmion scattering in chiral magnets. *Phys. Rev. B* **90**, 094423 (2014).
44. Vansteenkiste, A. et al. The design and verification of MuMax3. *AIP Adv.* **4**, 10 (2014).
45. Thiele, A. A. Steady-state motion of magnetic domains. *Phys. Rev. Lett.* **30**, 230 (1973).
46. Papanicolaou, N. & Tomaras, T. N. Dynamics of magnetic vortices. *Nucl. Phys. B* **360**, 425 (1991).
47. Kuchkin, V. M., Bessarab, P. F. & Kiselev, N. S. Thermal generation of droplet soliton in chiral magnet. *Phys. Rev. B* **105**, 184403 (2022).
48. Donahue, M. J. & McMichael, R. D. Exchange energy representations in computational micromagnetics. *Physica B: Condensed Matter* **223**, 272–278 (1997).

Acknowledgements

We acknowledge financial support from the National Research Fund Luxembourg under Grant No. CORE C22/MS/17415246/DeQuSky, the Icelandic Research Fund (Grant No. 217750), the University of Iceland Research Fund (Grant No. 15673), the Swedish Research Council (Grant No. 2020-05110), the Crafoord Foundation (Grant No. 20231063), the European Research Council (ERC) under the European Union's Horizon 2020 research and innovation program (Grant No. 856538, project "3D MAGiC"), and the ERC under the European Union's Horizon Europe research and innovation program (Grant No. 101078061, Project "SINGinGR").

Author contributions

V.M.K. and B.B.S. provided an analytical study. V.M.K. conducted micromagnetic simulations. V.M.K. and N.S.K. prepared the manuscript with substantial assistance from other authors. V.M.K., N.S.K., B.B.S., and P.F.B. reviewed and commented on the manuscript.

Funding

Open Access funding enabled and organized by Projekt DEAL.

Competing interests

The authors declare no competing interests.

Additional information

Supplementary information The online version contains supplementary material available at https://doi.org/10.1038/s42005-024-01913-1.

Correspondence and requests for materials should be addressed to Vladyslav M. Kuchkin or Nikolai S. Kiselev.

Peer review information *Communications Physics* thanks Xiansi Wang and the other, anonymous, reviewer(s) for their contribution to the peer review of this work. A peer review file is available.